

<https://doi.org/10.1038/s41699-024-00473-w>

# Controlled epitaxy and patterned growth of one-dimensional crystals via surface treatment of two-dimensional templates

Check for updates

Myeongjin Jang<sup>1,2,5</sup>, Minseol Kim<sup>1,5</sup>, Sol Lee<sup>1,2</sup>, Minseok Kwon<sup>3</sup>, Hani Kang<sup>1</sup>, Kihyun Lee<sup>1,2</sup>, Jinsub Park<sup>1</sup>, Anh Tuan Hoang<sup>4</sup>, Jong-Hyun Ahn<sup>4</sup>, Yangjin Lee<sup>1,2</sup> & Kwanpyo Kim<sup>1,2</sup> ✉

Mixed-dimensional van der Waals (vdW) heterostructures offer promising platforms for exploring interesting phenomena and functionalities. To exploit their full potential, precise epitaxial processes and well-defined heterointerfaces between different components are essential. Here, we control the growth of one-dimensional (1D) vdW microwires on hexagonal crystals via plasma treatment of the growth templates. AgCN serves as a model 1D system for examining the dependence of the nucleation and growth parameters on the surface treatment conditions and substrate types. The oxygen-plasma-treated transition metal dichalcogenides form step edges mediated by formation of surface metal oxides, leading to robust AgCN epitaxy with an enhanced nucleation density and low horizontal growth rates. Monte Carlo simulations reproduce the experimentally observed growth behaviors and unveil the crucial growth parameters, such as surface diffusivity. The plasma treatment results in distinct effects on graphite and hexagonal boron nitride templates, which undergo plasma-induced amorphization and deactivation of the AgCN vdW epitaxy. We achieve the selective growth of AgCN microwires on graphite using the deactivated vdW epitaxy. This study offers significant insights into the impact of surface treatment on 1D vdW epitaxy, opening avenues for controlled fabrication of mixed-dimensional vdW heterostructures.

Mix-dimensional van der Waals (vdW) heterostructures have recently garnered significant attention owing to their potential to reveal controlled physical properties and achieve advanced functionalities<sup>1–3</sup>. The interplay between the components present in vdW heterostructures exhibit various interesting behaviors, such as vdW epitaxy, interfacial structural reconstruction, and electrical and chemical modification via charge transfer or other processes<sup>4–11</sup>. Two-dimensional (2D) crystals have shown high compatibility with other materials and have emerged as excellent hosts for the formation of various vdW heterostructures<sup>6,10,12,13</sup>. In particular, through vdW epitaxy, 2D crystals can serve as superior templates for obtaining high-quality vdW heterostructures without encountering the lattice mismatch problem. Owing to these advantages, 2D crystals allow epitaxial growth of other 2D crystals<sup>14,15</sup>, various metallic films<sup>11,16</sup>, and semiconductors<sup>17,18</sup> with clean interfaces, enabling various interesting applications.

In-depth investigations are required to reveal the effect of surface defects in growth templates on the epitaxial process. Various defects that

reside in 2D crystals, such as vacancies, surface residues, and grain boundaries, tremendously affect the physical and chemical properties of these 2D crystals<sup>19–21</sup>. Previous studies have also shown that the assembly behaviors of atoms and molecules can be tuned by modifying the properties of their host surface<sup>22–25</sup>. Because the pristine surface of 2D crystals do not contain dangling bonds, the defects present in these crystals govern the growth modes of materials on these 2D surface<sup>26</sup>. Therefore, investigation of the vdW epitaxial process on surface-modified 2D crystals, can enhance our understanding of the role of defects in vdW epitaxy. Moreover, tuning the vdW epitaxy behavior is conducive to achieving tailored surface patterns for diverse applications.

In this study, we controlled the growth behaviors of one-dimensional (1D) vdW microwires via surface treatment of various hexagonal crystal templates. Recently, various types of 1D-2D vdW heterostructures have emerged as exciting platforms to induce interesting phenomena with potential in device applications<sup>27–30</sup>. AgCN microwires were adopted as

<sup>1</sup>Department of Physics, Yonsei University, Seoul, Republic of Korea. <sup>2</sup>Center for Nanomedicine, Institute for Basic Science (IBS), Seoul, Republic of Korea.

<sup>3</sup>Graduate Program of Semiconductor Science and Engineering, Yonsei University, Seoul, Republic of Korea. <sup>4</sup>School of Electrical and Electronic Engineering, Yonsei University, Seoul, Republic of Korea. <sup>5</sup>These authors contributed equally: Myeongjin Jang, Minseol Kim. ✉e-mail: [kpkim@yonsei.ac.kr](mailto:kpkim@yonsei.ac.kr)

model 1D systems to investigate the effect of surface treatment conditions and substrate types on nucleation and growth parameters. Oxygen plasma treatment on transition metal dichalcogenides (TMDCs) induced surface oxidation and formation of step edges. With plasma treatments, we observed the increased nucleation density and the reduced horizontal growth rates of AgCN microwires. Monte Carlo simulations reproduced the experimentally observed growth behavior and uncovered crucial growth parameters, such as surface diffusivity. Moreover, graphite and hexagonal boron nitride (h-BN) templates underwent amorphization due to the plasma treatment, and the vdW epitaxy of the AgCN assembly was deactivated. Thus, through the controlled deactivation of vdW epitaxy and patterned plasma treatment, we successfully selectively grew AgCN microwires on graphite. The results enhance our understanding of the surface treatment effect on 1D vdW epitaxy, and the proposed process is expected to facilitate controlled fabrication of mixed-dimensional vdW heterostructures for various interesting applications.

## Results and discussion

AgCN is a wide bandgap semiconductor with closely-packed atomic chains composed of  $[\text{Ag}-\text{C}\equiv\text{N}]_n$ <sup>31–33</sup>. In this study, AgCN serves as a model 1D vdW system, which displays a directional assembly behavior on 2D crystals. Previous studies demonstrated that AgCN displays an oriented vdW assembly behavior, wherein the substrate crystal symmetry governs the directions of the AgCN wire axis<sup>33–38</sup>. We employed low-power oxygen plasma treatment to modify the surface of various 2D templates and tune the

AgCN growth behavior (please refer to Methods and Supplementary Fig. 1 for detailed information on the plasma treatment and growth process).

Figure 1 shows the effect of plasma treatment on the vdW epitaxy of the AgCN microwires on WS<sub>2</sub>, a representative TMDC template. The optical and scanning electron microscopy (SEM) images confirm the aligned assembly of the AgCN microwires on the pristine WS<sub>2</sub> substrate (Fig. 1a, d). The axis of the AgCN microwires represents the molecular chain  $[\text{Ag}-\text{C}\equiv\text{N}]_n$  directions in the AgCN crystals, and the three-fold directions (orange arrows in Fig. 1d) correspond to the zigzag lattice directions of the underlying 2D substrate<sup>33</sup>. Fig. 1b, c show the AgCN assembled on the plasma-treated WS<sub>2</sub> substrate for 10 s under powers of 10 and 30 W, respectively. Evidently, the behavior of the AgCN assembly is modified by the plasma treatment. Although the assembled morphology and density of the wires are affected, the oriented vdW epitaxy of AgCN is maintained even with the plasma treatment, as evidenced by the observed three-fold axis of assembled AgCN in Fig. 1b, c, e, f.

The assembled microwires with 30 W plasma treatment require in-depth characterizations owing to their shortened assembled morphology. To precisely analyze the azimuthal angle distribution of the AgCN microwires and perform detailed structural characterizations, we employed the transmission electron microscopy (TEM) and selected-area electron diffraction (SAED) techniques, which allowed direct visualization of the relative orientations between WS<sub>2</sub> and the AgCN sub-microwire axis, as demonstrated in Fig. 1g–j<sup>33,38</sup>. Figure 1g displays a scanning transmission electron microscope (STEM) image of the shortened AgCN microwires on

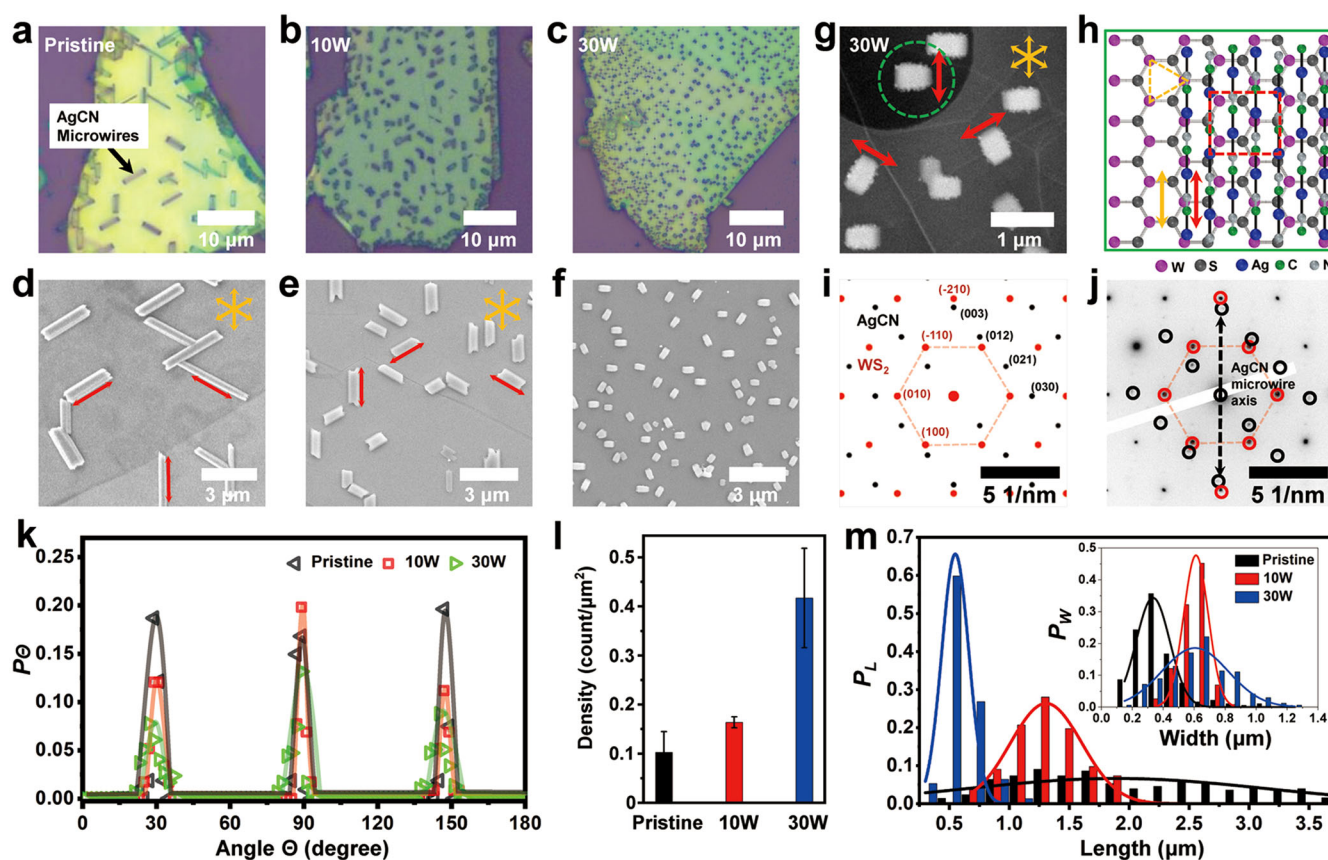


**Fig. 1** | Effect of plasma-treatment on the vdW epitaxy of the AgCN microwires. **a–c** Optical images of the AgCN microwires grown on WS<sub>2</sub> depending on the oxygen plasma treatment condition (pristine, 10 and 30 W). **d–f** SEM images of the AgCN microwires on WS<sub>2</sub> depending on the oxygen treatment condition (pristine, 10 and 30 W). The red and orange arrows represent the molecular chain directions of AgCN aligned along the zigzag lattice of the substrate. **g** STEM image of the AgCN microwires grown on plasma-treated WS<sub>2</sub> (30 W power). The red and orange arrows indicate the AgCN molecular chain directions. **h** Atomic model of the AgCN

microwires grown on WS<sub>2</sub>. **i** Simulated SAED pattern of AgCN on WS<sub>2</sub>. **j** Experimental SAED pattern of AgCN grown on WS<sub>2</sub>. The diffraction signals of AgCN and WS<sub>2</sub> are marked with black and red circles, respectively. **k** Histogram of the azimuthal distributions of the AgCN chain directions (red arrows) on pristine and plasma-treated WS<sub>2</sub>. **l** Density of the AgCN microwires grown on pristine and plasma-treated WS<sub>2</sub>. The error bars indicate the standard deviation from 10 to 15 samples. **m** Length distribution of the AgCN microwires grown on pristine and plasma-treated WS<sub>2</sub>. The inset shows the width distribution of the AgCN microwires.

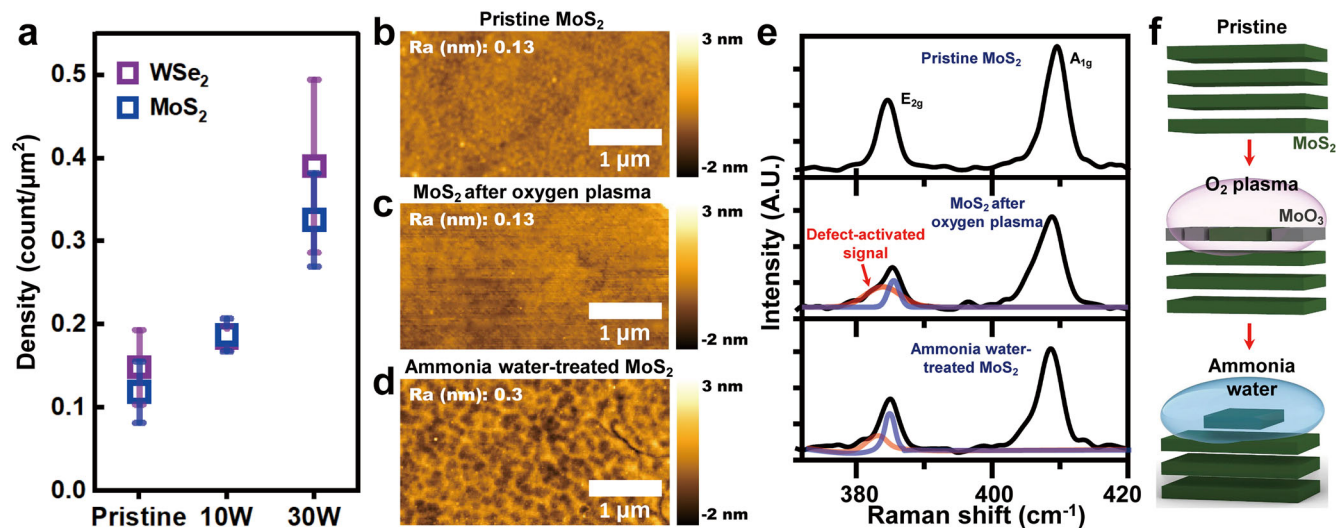


**Fig. 2 | Surface modification of the TMDCs via oxygen plasma and treatment with the AgCN growth solution. a** The density of the AgCN microwires grown on  $\text{MoS}_2$  and  $\text{WSe}_2$  under different plasma treatment conditions. The error bars indicate the standard deviation from 10 to 15 samples. **b–d** AFM topography images of pristine, plasma-treated, and ammonia water-treated  $\text{MoS}_2$ . **e** Raman spectra of

pristine, plasma-treated, and ammonia water-treated  $\text{MoS}_2$ ; the metal oxide is marked with a red signal. **f** Schematics showing the effect of plasma treatment and ammonia water during the AgCN growth. The oxygen plasma treatment leads to the formation of a surface metal-oxide layer, and ammonia water selectively removes the metal oxide.

plasma-treated (30 W)  $\text{WS}_2$ . Figures 1h and i show atomic models of AgCN aligned on a  $\text{WS}_2$  substrate and their corresponding simulated SAED patterns. Figure 1j shows the experimental SAED pattern of the AgCN crystals grown on plasma-treated (30 W for 10 s)  $\text{WS}_2$ ; here, the  $\text{WS}_2$  and AgCN signals are shown using red and dark circles, respectively. The diffraction signals detected from both the materials are azimuthally well-aligned, confirming that the atomic axis of the AgCN crystal is parallel to the zigzag direction of  $\text{WS}_2$ . Interestingly, the correlation between the real-space image and SAED patterns confirms that the short side corresponds to the molecular chain axis (black dashed arrows)<sup>38</sup>. Figure 1k shows a histogram of the azimuthal angle distributions of the AgCN molecular chain directions under different surface conditions of  $\text{WS}_2$  (pristine in black, 10 W in red, and 30 W in green); this figure clearly shows the robustness of the aligned growth even after the plasma treatment.

Although the oriented epitaxy of AgCN is maintained after the plasma treatment of the TMDC templates, the plasma treatment modifies the growth behavior of AgCN. In particular, compared to the growth behavior on pristine  $\text{WS}_2$ , the nucleation density and morphology of the assembled microwires change after the plasma treatment. After plasma treatment at 10 W power for 10 s, the nucleation density (Fig. 1l) becomes approximately twice that on the pristine  $\text{WS}_2$ , while the length of the wires significantly decreases compared to that on the pristine  $\text{WS}_2$  (Fig. 1m). Upon plasma treatment at 30 W, the nucleation density undergoes a five-fold increase compared to that in the pristine case (Fig. 1l). The average length decreases further (Fig. 1m), while the width remains relatively stable (inset of Fig. 1m). Consequently, the aspect ratio of the grown wires decreases further, as shown in Supplementary Fig. 2. A similar plasma-treatment effect is observed on the AgCN vdW epitaxy on other TMDC substrates. For example, an increased nucleation density and shortened wire morphology are observed after plasma treatment on  $\text{MoS}_2$  and  $\text{WSe}_2$ , as shown in Fig. 2a and Supplementary Figs. 2 and 3.

We evaluated the changes in the plasma-treated TMDC surfaces to understand the AgCN growth modification universally observed on TMDCs. We monitored the surfaces of the TMDC substrates at different stages of the sample fabrication procedure using atomic force microscopy (AFM) imaging and Raman spectroscopy techniques, and the corresponding results are shown in Fig. 2b–e. The AFM images show that the  $\text{O}_2$  plasma treatment (power 30 W) does not induce a noticeable change in the surface roughness of  $\text{MoS}_2$  (Fig. 2c, d). On the other hand, the Raman spectra displays peaks corresponding to distinct vibrational modes of

$\text{MoS}_2$ <sup>39,40</sup> and those of  $\text{MoO}_3$  after the  $\text{O}_2$  plasma treatment as shown in Fig. 2e. The observed formation of  $\text{MoO}_3$  from the  $\text{O}_2$  plasma is consistent with the results of previous studies<sup>41</sup>. Previous reports indicate that Ar precursor results in etching of layers<sup>42</sup>, whereas  $\text{O}_2$  precursor transforms a few surface layers of  $\text{MoS}_2$  into oxide layers such as  $\text{MoO}_3$ <sup>41,43,44</sup>. The absence of a noticeable surface roughness can be attributed to atomically flat  $\text{MoO}_3$ , which is formed by the reaction of  $\text{MoS}_2$  with  $\text{O}_2$ .

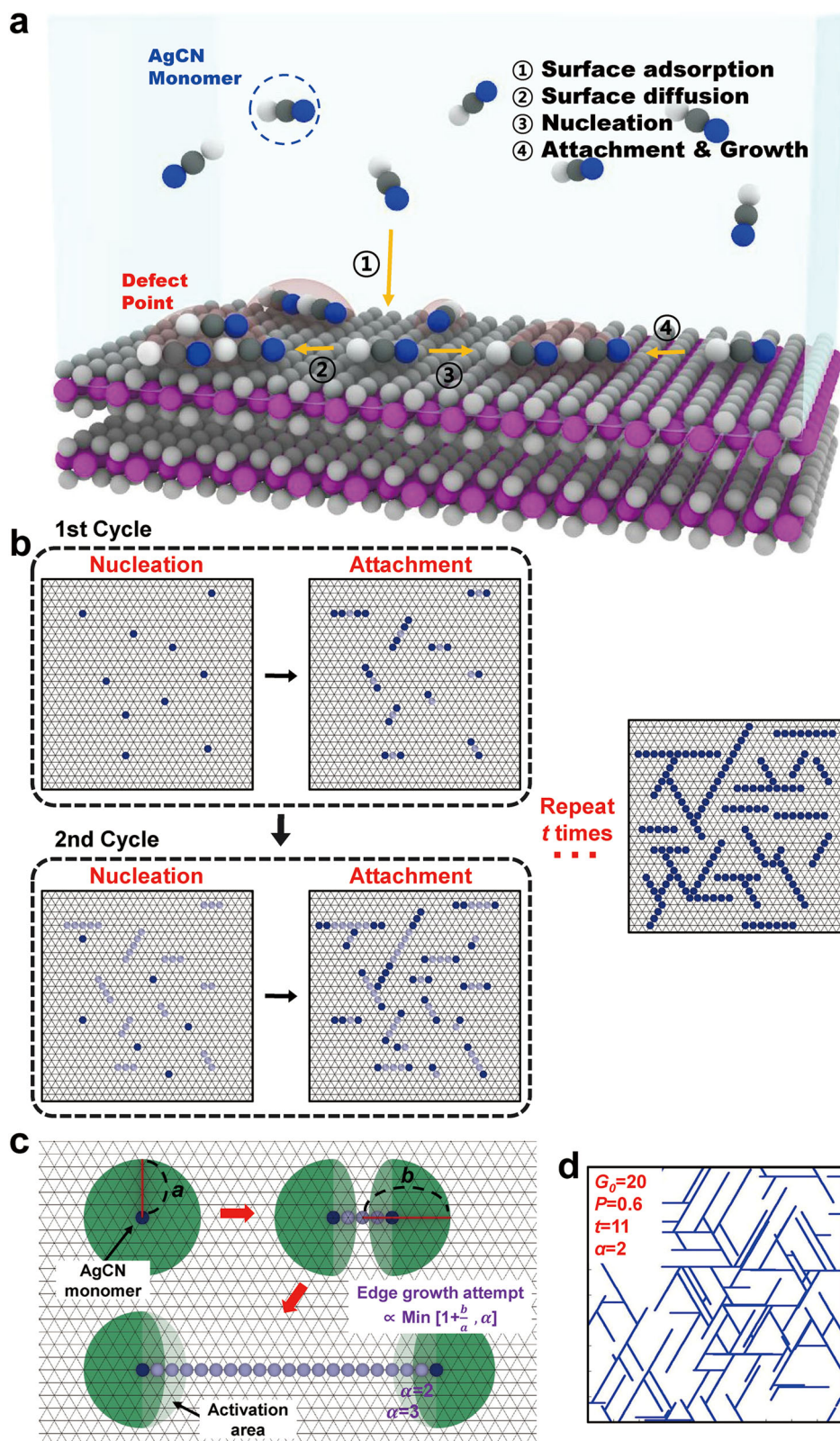
The metal oxide formed during the  $\text{O}_2$  plasma treatment undergoes further chemical reactions under the AgCN growth environment. AgCN is grown by drop-casting an AgCN solution in ammonia water.  $\text{MoO}_3$  reacts with ammonia and forms water-soluble ammonium molybdate<sup>45</sup>. The surface roughness drastically increases owing to the removal of  $\text{MoO}_3$  after the ammonia water treatment, as shown in Fig. 2d. By TEM analysis, we directly confirmed the effect of oxygen plasma treatment on TMDC templates. As shown in Supplementary Fig. 4, dark field (DF) TEM analysis and atomic resolution STEM imaging with  $\text{MoS}_2$  samples revealed that the plasma treatment leads to sample thinning and the generation of step edges. Therefore, compared to the pristine surface, the plasma-treated TMDC templates show a large number of step edges and high surface roughness, as indicated in Fig. 2f. This increase in the number of surface defects<sup>22</sup> can modify the assembly behaviors of AgCN. Conversely, the surface of TMDC still maintains the overall hexagonal lattice during the surface treatment (Supplementary Fig. 4d) and can host the observed persistent oriented vdW epitaxy.

The general heteroepitaxy on the surface usually occurs in the following steps: (1) surface adsorption of monomers, (2) diffusion on the surface, (3) nucleation of a crystallite, and (4) attachment of monomers and growth of crystallites (Fig. 3a)<sup>22,46,47</sup>. According to the general nucleation theory<sup>22,47</sup>, when the size of an AgCN crystallite reaches a particular critical value, stable nucleation events occur. In our experiments, the AgCN monomer dissolved in the solvent was adsorbed onto the surface of the 2D crystal templates and subsequently exhibited surface diffusion or desorption via the above-mentioned processes. The surface defects, such as vacancy or step edges, can promote AgCN nucleation via a heterogeneous nucleation process. On the other hand, on a surface with a significant number of defects, the subsequent attachment process of monomers may be slowed down due to the reduced monomer diffusivity resulting from elevated energy barriers associated with detrapping from defects<sup>22</sup>.

To evaluate the nucleation and lateral growth behavior of the AgCN microwires on the TMDC templates, Monte Carlo simulations were

**Fig. 3 | Monte Carlo simulation of the AgCN microwire growth on a hexagonal 2D substrate.**

**a** Schematic showing the atomic-scale AgCN microwire growth process on a 2D substrate. ① Surface adsorption of AgCN monomers. ② Diffusion of AgCN monomers on the substrate. ③ Nucleation of AgCN crystals. ④ Horizontal growth of AgCN wires from the monomer attachments. **b** Schematics of the growth simulation process. Individual growth cycles compose of nucleation and growth steps based on the growth mode along the hexagonal lattice directions. Cycles are repeated  $t$  times to reach the final configurations. **c** Schematic showing the growth parameters. The growth is set to be proportional to the effective area (green regions) related to the edge growth. **d** Exemplary simulation results with given growth parameters.



performed, and the results were compared with those of the experiments<sup>48</sup> (details of the simulation process are provided in the Methods section). Figure 3b shows the overall simulation process of the AgCN growth on the hexagonal lattice, in which the AgCN wires can occupy individual lattice points. In our simulation, each cycle is composed of nucleation and subsequent attachment steps, with total  $t$  cycles. The number of nucleation

events per cycle, number of attachment attempts, and probability of a successful attachment are the crucial simulation parameters. We assume that although the nucleation occurs at random sites, the pre-existing nucleation sites deactivate the nearby nucleation events for a certain lattice distance (parameter  $a$ )<sup>49</sup>. The number of nucleation events per cycle (from the first cycle to the  $t_{th}$  cycles) is considered a Gaussian distribution, as

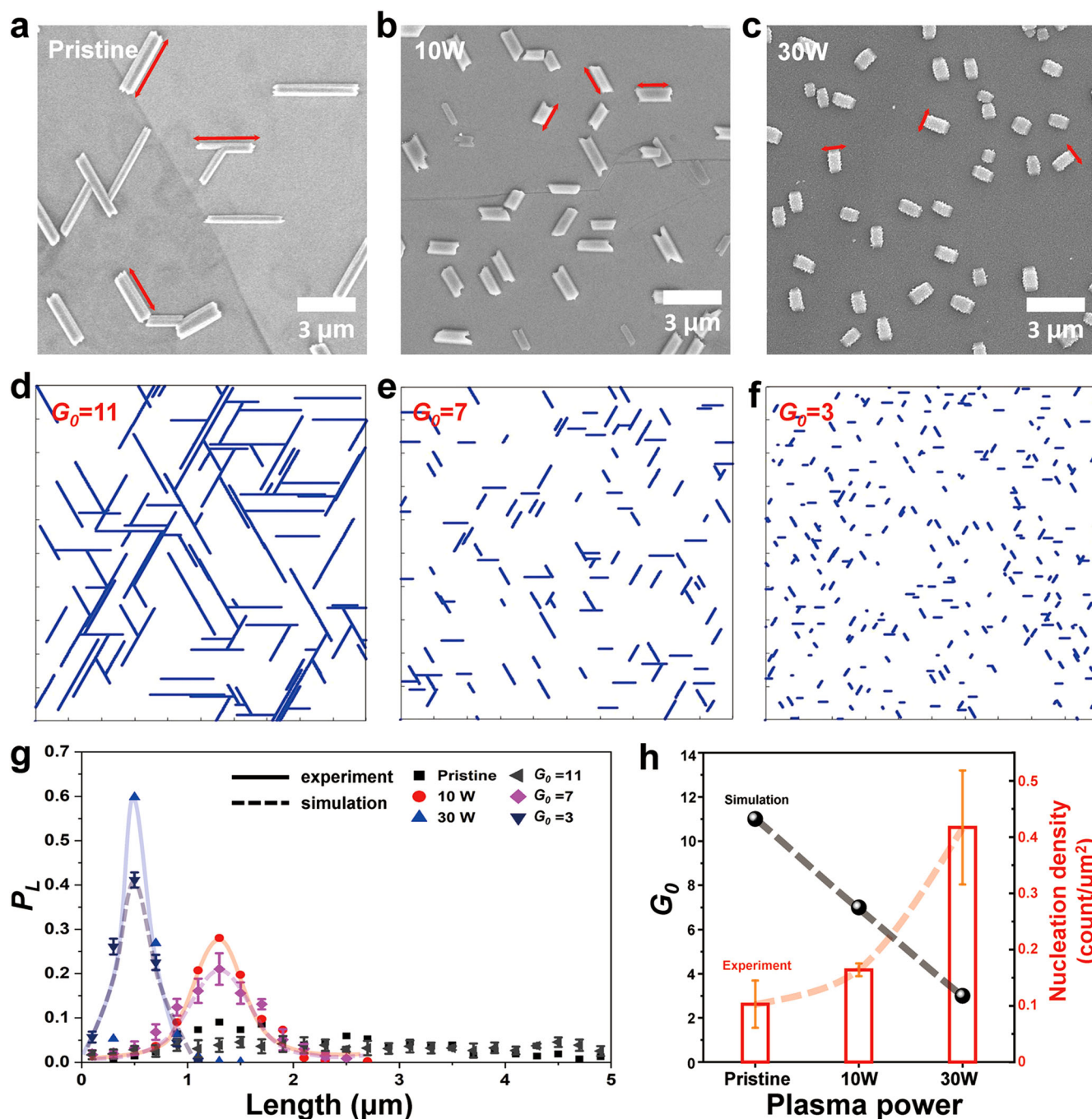


**Fig. 4 | Comparison between the experimental and simulation results of the AgCN microwire growth behavior.** a–c SEM images of the AgCN microwires grown on pristine and plasma-treated WS<sub>2</sub>. d–f Simulation results obtained with various simulation parameters. The simulation results shown in d–f correspond to  $G_0 = 11, 7$ , and 3, respectively. Other parameter conditions;  $P = 0.6, \alpha = 2$ .

**g** Comparison between the experimental and simulated AgCN microwire length distributions. The error bars indicate the standard deviation from 10 simulations. **h** Identified  $G_0$  value and the experimental nucleation density. The error bars indicate the standard deviation from 10 ~ 15 samples.

shown in Supplementary Fig. 5, to reflect the mild-heating-induced growth phenomena of AgCN. The nucleated crystallites undergo subsequent attachments, and the direction of the horizontal growth is randomly assigned at the first growth stage of a crystallite. Once the growth direction is set, horizontal elongation is allowed, with two wire ends serving as the growth fronts. The number of growth attempts per cycle is expressed as  $G_0 \min(1 + \frac{b}{a}, \alpha)$ , and the probability for a successful growth is  $P$  (value between 0 and 1). The function  $\min(1 + \frac{b}{a}, \alpha)$  modifies the number of growth attempts as a function of the crystallite size (Fig. 3c), and  $G_0$  is a constant related to surface diffusivity. In particular, we assume that the

effective area (green color in Fig. 3c) for the successful edge-mediated growth, and the area near the central region of the wires does not contribute to the edge-mediated growth. In summary, the average number of attachments per cycle is given by  $G_0 P \min(1 + \frac{b}{a}, \alpha)$ , and an exemplary result is shown in Fig. 3d.

The effects of various growth parameters on the growth behaviors were systematically evaluated.  $G_0, P, \alpha$ , and  $t$  were varied to observe the changes in the length distribution as shown in Supplementary Fig. 6, and these simulated distributions were compared with the experimental observations to elucidate the crucial growth parameters and their effects. Figure 4a–c shows

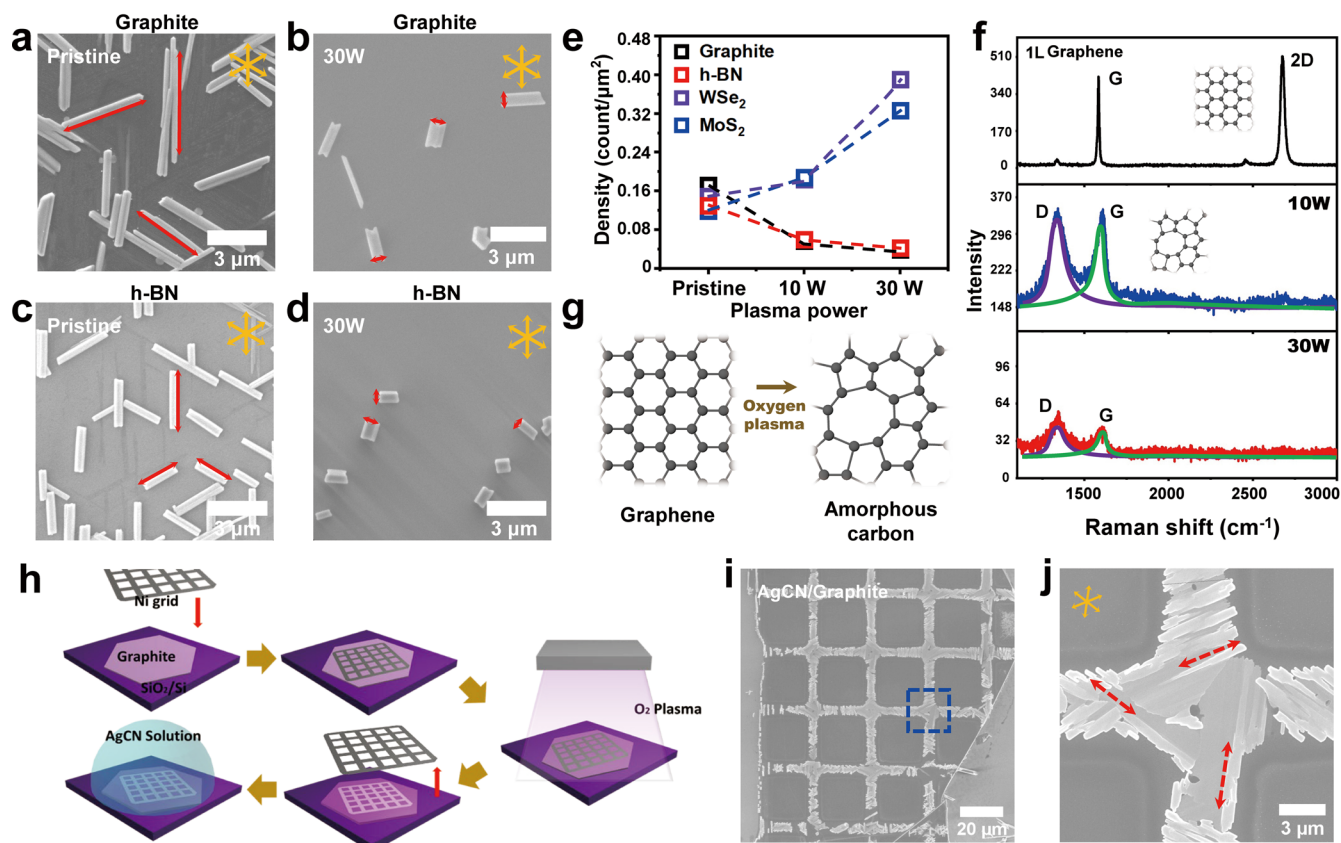


**Fig. 5 | Deactivation of vdW epitaxy by plasma treatment and patterned growth of AgCN microwires on graphite and h-BN.** **a, c** SEM image of the AgCN microwires grown on pristine graphite and h-BN, respectively. **b, d** SEM image of the AgCN microwires grown on plasma-treated graphite and h-BN, respectively (30 W power for 10 s). **e** Density of the AgCN microwires grown on various 2D substrates with different plasma-treatment conditions. **f** Raman spectra of pristine and plasma-

treated monolayer graphene. **g** Schematics showing the amorphization of graphene by plasma treatment. **h** Schematics showing the patterned growth of AgCN microwires on graphite or h-BN. **i** SEM image showing the patterned growth of AgCN microwires on graphite. **j** Zoomed-in SEM image of the blue dashed box in panel 5i. The red and orange arrows indicate the three AgCN wire axes.

the experimental results obtained for the pristine sample at different plasma powers of 10 and 30 W. Figure 4d–f presents the exemplary simulation results, which are in good agreement with the experimental ones. As summarized in Fig. 4g, the simulated and experimentally observed wire length distributions are in good agreement with each other. Interestingly, we identified a critical correlation between the growth attempt and nucleation number. In particular, the identified growth attempt parameter ( $G_0$ ) is reduced by a factor of approximately 3–4 for the 30-W-plasma-treated samples, whereas the number of nucleation sites increase by a factor of approximately 3 compared to the pristine case (inset of Fig. 4h). The anti-correlation between  $G_0$  and the nucleation density is consistent with our understanding that the surface defects increase the nucleation probability but decrease the surface diffusion. We also observed that the used number of cycles ( $t$ ) display an anti-correlation with  $G_0$ . This can be attributed to the early consumption (smaller  $t$ ) of the growth material under the faster diffusion case (larger  $G_0$ ).

Chemical vapor deposition (CVD) process has emerged as effective way to produce high-quality large-area TMDC samples<sup>50–54</sup>. The confirmation of AgCN microwire growth on CVD TMDC samples is also an interesting subject. Furthermore, the charge transfer behavior between AgCN and monolayer TMDC provided by CVD method can be studied efficiently. We confirmed the successful growth of AgCN microwires on metal-organic CVD (MOCVD) monolayer MoS<sub>2</sub> substrate as shown in Supplementary Fig. 7. The morphology of AgCN microwires bears some resemblance to those observed on plasma-treated mechanically-exfoliated TMDC samples. The utilized MOCVD MoS<sub>2</sub> samples have the grain size of approximated 1  $\mu\text{m}$ <sup>53</sup>, and the presence of grain boundaries can play a role

similar to those of step edges and other types of defects induced by plasma effect. We also confirmed that there is a charge transfer between AgCN microwires and MoS<sub>2</sub> by photoluminescence (PL) measurement as shown in Supplementary Fig. 7c–h. The slight blue shift in PL position and the increased exciton signal suggest the reduced *n*-doping of MoS<sub>2</sub> by the electron transfer from MoS<sub>2</sub> to AgCN<sup>55,56</sup>.

The effect of the plasma treatment on the graphite and h-BN substrates is significantly different from that on the TMDC substrates. The SEM images of the AgCN microwires grown on pristine and plasma-treated graphite and h-BN are shown in Fig. 5a–d. Unlike the case of the TMDC substrates, the nucleation density of the AgCN microwires grown on graphite and h-BN significantly decreases after the plasma treatment (Fig. 5e). To characterize the plasma treatment effect, we measured the Raman spectra of monolayer graphene before and after the plasma treatment (10 and 30 W), and the measured spectra are displayed in Fig. 5f. The Raman spectrum of pristine 1 L graphene shows G and 2D peaks. After the plasma treatment, the 2D peak disappears, while the G peak broadens, and a D peak appears. Overall, the Raman spectrum of plasma-treated graphene indicates the generation of defective graphene (i.e., amorphization) due to the oxygen plasma treatment (Fig. 5g)<sup>57,58</sup>. Because of the utilized plasma conditions, the graphene surface becomes amorphous with a thickness of minimum two layers, because bilayer graphene also undergoes a similar degree of amorphization as monolayer graphene (Supplementary Fig. 8). The amorphized graphene is robust against the ammonia water treatment owing to its high chemical stability, which is different from the behavior of metal oxides. Therefore, the amorphized surface of graphene due to the plasma treatment explains the deactivation of the AgCN microwire epitaxy. A similar

deactivation behavior is observed on the plasma-treated h-BN and can be also attributed to the generation of a defective h-BN surface<sup>59,60</sup>.

Finally, we demonstrate the patterned growth of AgCN on selected regions via the deactivation of vdW epitaxy with plasma treatment on graphite. Figure 5h schematically shows the process for patterned AgCN microwire growth. This process includes (1) placement of a mesh grid on exfoliated graphite, (2) oxygen plasma treatment (30 W for 10 s), and (3) AgCN growth. A TEM grid was utilized as a patterning mesh in our study. The recorded AFM images show that the phase signals detected from the plasma-treated regions are different from those detected from the regions protected from the plasma treatment (Supplementary Fig. 9); this result implies that the surface property changes owing to the amorphization. Figure 5i, j shows the SEM images of the patterned AgCN microwires, which are assembled only on the regions protected from the plasma treatment. The zoomed-in SEM image in Fig. 5j also indicates close packing of the AgCN microwires with tri-axial oriented epitaxy.

In summary, we controlled the growth process of 1D vdW microwires via surface treatment of various hexagonal crystal templates. The oxygen plasma treatment on the TMDC substrates resulted in the increased nucleation density and the reduced horizontal growth rates of AgCN assembly. Monte Carlo simulations reproduced the experimental growth results and unraveled important parameters, including surface diffusivity. Interestingly, the plasma treatment on graphite and h-BN deactivated the AgCN microwire vdW epitaxy due to the amorphization of the substrate. Using the deactivation of vdW epitaxy, we achieved selective growth of AgCN microwires on graphite through patterned plasma treatment. The family of 1D metal cyanides shows distinct assembly morphologies and electrical/optical properties depending on types of metals (Au, Ag, Cu, etc.) in cyanides<sup>32–34,38</sup>. The observed charge transfer behavior between 2D substrate and 1D metal cyanides also demonstrate the potential utility of 1D chains in various vdW platforms including other types of 2D crystals<sup>16,29,38,61,62</sup>. This study highlights the intricate mechanisms underlying the surface treatment of 2D templates for realizing 1D vdW epitaxy as well as paves the way for controlled fabrication of mixed-dimensional vdW heterostructures for various applications.

## Methods

### AgCN microwire growth and plasma treatment

Single-crystal graphite, h-BN, and TMDCs (MoS<sub>2</sub>, WS<sub>2</sub>, and WSe<sub>2</sub>) were purchased from HQ Graphene. Monolayer MoS<sub>2</sub> samples were synthesized by metal-organic CVD process, and the detailed description on the growth process can be found elsewhere<sup>53</sup>. CVD graphene was synthesized on polycrystalline Cu foil with CH<sub>4</sub> at low pressure<sup>63,64</sup>. These crystals were mechanically exfoliated onto 280-nm-thick-SiO<sub>2</sub>/Si substrates. AgCN microwires were grown on the exfoliated 2D crystals using the previously developed drop-cast method<sup>33</sup>. Briefly, a solution of AgCN (1–2 mM) was prepared by dissolving AgCN (99%, Sigma-Aldrich) in an ammonia solution (100 mL, 14.8 M, Samchun). Using a micropipette, 1.5 μL of the AgCN solution was dropped onto the target 2D crystals on the SiO<sub>2</sub>/Si wafers. Mild heating on a hot-plate at 85 °C was performed for 15 min in air. Prior to the AgCN growth, some 2D crystals were subjected to O<sub>2</sub> plasma treatment for 10 s at 10 or 30 W under a pressure of  $3.6 \times 10^{-1}$  Torr using a radio-frequency plasma cleaner (COVANCE/CUTE, Femto Science Inc.). For the patterned growth of AgCN microwires, a TEM grid (Ni mesh, 1500 slim bar, SPI supplies) was placed on the exfoliated 2D crystals to partially protect the surface of the 2D crystal from the plasma.

### Characterizations

Optical microscopy images were acquired using Leica DM-750M. SEM images were obtained using JEOL-JSM-7900F and JEOL-7016F-PLUS operated at 5 or 10 kV. SAED, DF imaging, and atomic-resolution HAADF-STEM were obtained with JEOL 2100Plus operated at 200 kV

and spherical aberration-corrected JEOL ARM-200F operated at 80 kV. The analysis of Raman spectra was obtained with MOCVD MoS<sub>2</sub> and CVD graphene samples at room temperature using a Raman spectrometer (Horiba) with an ND:Yag laser (532 nm). AFM images were obtained in non-contact mode using the Park XE7 atomic force microscope at a scan speed of 48 μm/s with a silicon cantilever (ppp-nchr, Nanosensors). PL measurement was performed at room temperature using a laser with a wavelength of 532 nm from Nanobase XperRF.

### Simulations

Monte Carlo simulations were performed using MATLAB R2021a-based home-built codes. A hexagonal mesh substrate was used to model the tri-axial 1D growth mode of AgCN. Each growth step was composed of (1) random nucleation of wires and (2) horizontal growth of wires along the hexagonal mesh. The total number of wire nuclei were adapted from the experimental results, and Gaussian distributed nucleation events were assumed for each growth step (Supplementary Fig. 5). All the existing and newly added nucleation sites underwent edge-mediated growth via the growth attempts with a certain probability. For the growth, we assumed that the AgCN monomers need to land on a certain region (green regions in Fig. 3c) of the substrate and diffuse to the edge location. For each growth step, the number of growth attempts was modeled as  $G_0 \min(1 + \frac{b}{a}, \alpha)$ , and the probability for a successful growth was denoted by  $P$  (value smaller than 1). Here,  $a$ ,  $b$ , and  $\alpha$  are constants related to the effective landing area, and  $G_0$  is a constant related to the diffusion process. When the edge growth front of a wire met another wire, the growth was terminated as observed in the experiment. The growth step (nucleation and growth) was proceeded for  $t$  times. The parameter ranges used in the simulations were:  $a = 3 \sim 4$  lattices,  $b = a + L$  ( $L$  is the length of a given wire),  $\alpha = 2 \sim 4$ , and  $G_0 = 2 \sim 15$ .

### Data availability

The authors declare that the data supporting the findings are available within the paper and its supplementary information. The corresponding authors can also provide data upon reasonable request.

### Code availability

Upon request, authors will make available any previously unreported computer code used to generate results that are reported in the paper.

Received: 14 November 2023; Accepted: 25 April 2024;

Published online: 16 May 2024

## References

- Geim, A. K. & Grigorieva, I. V. Van der Waals heterostructures. *Nature* **499**, 419–425 (2013).
- Jariwala, D., Marks, T. J. & Hersam, M. C. Mixed-dimensional van der Waals heterostructures. *Nat. Mater.* **16**, 170–181 (2017).
- Liu, Y., Huang, Y. & Duan, X. Van der Waals integration before and beyond two-dimensional materials. *Nature* **567**, 323–333 (2019).
- Yoo, H. et al. Atomic and electronic reconstruction at the van der Waals interface in twisted bilayer graphene. *Nat. Mater.* **18**, 448–453 (2019).
- Weston, A. et al. Atomic reconstruction in twisted bilayers of transition metal dichalcogenides. *Nat. Nanotechnol.* **15**, 592–597 (2020).
- Shen, P.-C. et al. Ultralow contact resistance between semimetal and monolayer semiconductors. *Nature* **593**, 211–217 (2021).
- Wang, Y. et al. P-type electrical contacts for 2D transition-metal dichalcogenides. *Nature* **610**, 61–66 (2022).
- Regan, E. C. et al. Mott and generalized Wigner crystal states in WSe<sub>2</sub>/WS<sub>2</sub> moiré superlattices. *Nature* **579**, 359–363 (2020).
- Chen, G. et al. Tunable correlated Chern insulator and ferromagnetism in a moiré superlattice. *Nature* **579**, 56–61 (2020).
- Yang, J. et al. Self-organized growth and self-assembly of nanostructures on 2D materials. *FlatChem* **5**, 50–68 (2017).

11. Lee, Y. et al. Single-crystalline metallic films induced by van der Waals epitaxy on black phosphorus. *Chem. Mater.* **33**, 3593–3601 (2021).
12. Kim, Y. et al. Remote epitaxy through graphene enables two-dimensional material-based layer transfer. *Nature* **544**, 340–343 (2017).
13. Kum, H. S. et al. Heterogeneous integration of single-crystalline complex-oxide membranes. *Nature* **578**, 75–81 (2020).
14. Gong, Y. Vertical and in-plane heterostructures from WS<sub>2</sub>/MoS<sub>2</sub> monolayers. *Nat. Mater.* **13**, 1135–1142 (2014).
15. Le, C. T. et al. Negative valley polarization of the intralayer exciton via one-step growth of H-type heterobilayer WS<sub>2</sub>/MoS<sub>2</sub>. *ACS Nano* **17**, 2629–2638 (2023).
16. Lee, K. et al. Anisotropic assembly and reorganization of noble metals on black phosphorus van der Waals template. *Curr. Appl. Phys.* **51**, 98–103 (2023).
17. Lee, C.-H. et al. Epitaxial growth of molecular crystals on van der Waals substrates for high-performance organic electronics. *Adv. Mater.* **26**, 2812–2817 (2014).
18. Yun, T. K. et al. Commensurate assembly of C<sub>60</sub> on black phosphorus for mixed-dimensional van der Waals transistors. *Small* **18**, 2105916 (2022).
19. Cançado, L. G. et al. Quantifying defects in graphene via Raman spectroscopy at different excitation energies. *Nano Lett.* **11**, 3190–3196 (2011).
20. Erickson, K. et al. Determination of the local chemical structure of graphene oxide and reduced graphene oxide. *Adv. Mater.* **22**, 4467–4472 (2010).
21. Yu, Q. et al. Control and characterization of individual grains and grain boundaries in graphene grown by chemical vapour deposition. *Nat. Mater.* **10**, 443–449 (2011).
22. Zhang, Z. & Lagally, M. G. Atomistic processes in the early stages of thin-film growth. *Science* **276**, 377–383 (1997).
23. Liu, L. et al. Slow gold adatom diffusion on graphene: effect of silicon dioxide and hexagonal boron nitride substrates. *J. Phys. Chem. B* **117**, 4305–4312 (2013).
24. Kim, K. et al. Selective metal deposition at graphene line defects by atomic layer deposition. *Nat. Commun.* **5**, 4781 (2014).
25. Thomsen, J. D. et al. Suspended graphene membranes to control Au nucleation and growth. *ACS Nano* **16**, 10364–10371 (2022).
26. Barth, J. V., Costantini, G. & Kern, K. Engineering atomic and molecular nanostructures at surfaces. *Nature* **437**, 671–679 (2005).
27. Li, D. et al. Assembly of close-packed ferroelectric polymer nanowires via interface-epitaxy with ReS<sub>2</sub>. *Adv. Mater.* **33**, 2100214 (2021).
28. Tao, J.-J. et al. Fabrication of 1D Te/2D ReS<sub>2</sub> mixed-dimensional van der Waals p-n heterojunction for high-performance phototransistor. *ACS Nano* **15**, 3241–3250 (2021).
29. Lv, Q. et al. Ultrafast charge transfer in mixed-dimensional WO<sub>3-x</sub> nanowire/WSe<sub>2</sub> heterostructures for attomolar-level molecular sensing. *Nat. Commun.* **14**, 2717 (2023).
30. Fan, C. et al. Self-competitive growth of CsPbBr<sub>3</sub> planar nanowire array. *Nano Lett.* **24**, 3750–3758 (2024).
31. Bowmaker, G. A., Kennedy, B. J. & Reid, J. C. Crystal structures of AuCN and AgCN and vibrational spectroscopic studies of AuCN, AgCN, and CuCN. *Inorg. Chem.* **37**, 3968–3974 (1998).
32. Chippindale, A. M. et al. Mixed copper, silver, and gold cyanides, (M<sub>x</sub>M'<sub>1-x</sub>)CN: tailoring chain structures to influence physical properties. *J. Am. Chem. Soc.* **134**, 16387–16400 (2012).
33. Lee, Y. et al. Universal Oriented van der Waals epitaxy of 1D cyanide chains on hexagonal 2D crystals. *Adv. Sci.* **7**, 1900757 (2020).
34. Jang, M. et al. Unidirectional alignment of AgCN microwires on distorted transition metal dichalcogenide crystals. *ACS Appl. Mater. Interfaces* **13**, 8727–8735 (2021).
35. Ham, J., Lim, J., Hong, S. & Lee, W. C. Spin coating promotes the epitaxial growth of AgCN microwires on 2D materials. *ACS Nano* **16**, 20521–20532 (2022).
36. Lee, W. C. et al. Graphene-templated directional growth of an inorganic nanowire. *Nat. Nanotechnol.* **10**, 423–428 (2015).
37. Kim, J. et al. Precise identification of graphene's crystal structures by removable nanowire epitaxy. *J. Phys. Chem. Lett.* **8**, 1302–1309 (2017).
38. Jang, J. et al. One-dimensional assembly on two-dimensions: AuCN nanowire epitaxy on graphene for hybrid phototransistors. *Nano Lett.* **18**, 6214–6221 (2018).
39. Lee, C. et al. Anomalous lattice vibrations of single- and few-layer MoS<sub>2</sub>. *ACS Nano* **4**, 2695–2700 (2010).
40. Parkin, W. M. et al. Raman shifts in electron-irradiated monolayer MoS<sub>2</sub>. *ACS Nano* **10**, 4134–4142 (2016).
41. Ko, T. Y. et al. On-stack two-dimensional conversion of MoS<sub>2</sub> into MoO<sub>3</sub>. *2d Mater.* **4**, 014003 (2016).
42. Liu, Y. et al. Layer-by-layer thinning of MoS<sub>2</sub> by plasma. *ACS Nano* **7**, 4202–4209 (2013).
43. Yoon, A., Kim, J. H., Yoon, J., Lee, Y. & Lee, Z. Van der Waals epitaxial formation of atomic layered α-MoO<sub>3</sub> on MoS<sub>2</sub> by oxidation. *Mater. Interfaces* **12**, 22029–22036 (2020).
44. Reidy, K. et al. Atomic-scale mechanisms of MoS<sub>2</sub> oxidation for kinetic control of MoS<sub>2</sub>/MoO<sub>3</sub> interfaces. *Nano Lett.* **23**, 5894–5901 (2023).
45. Hallada, C. J. Phase diagram of the NH<sub>3</sub>-MoO<sub>3</sub>-H<sub>2</sub>O system. *J. Less-common Met.* **36**, 103–110 (1974).
46. Jensen, P., Barabási, A. L., Larralde, H., Havlin, S. & Stanley, H. E. Deposition, diffusion, and aggregation of atoms on surfaces: A model for nanostructure growth. *Phys. Rev. B* **50**, 15316–15329 (1994).
47. Syromyatnikov, A. G., Saletsky, A. M. & Klavysyuk, A. L. Distributions of atomic wire lengths. *Phys. Rev. B* **97**, 235444 (2018).
48. Hwang, W. & Eryilmaz, E. Kinetic signature of fractal-like filament networks formed by orientational linear epitaxy. *Phys. Rev. Lett.* **113**, 025502 (2014).
49. Han, Y. et al. Nucleation and growth kinetics for intercalated islands during deposition on layered materials with isolated pointlike surface defects. *Phys. Rev. Mater.* **1**, 053403 (2017).
50. Li, T. et al. Epitaxial growth of wafer-scale molybdenum disulfide semiconductor single crystals on sapphire. *Nat. Nanotechnol.* **16**, 1201–1207 (2021).
51. Wu, Q. et al. Resolidified chalcogen precursors for high-quality 2D semiconductor growth. *Angew. Chem. Int. Ed.* **62**, e202301501 (2023).
52. Cai, Z. et al. Dissolution-precipitation growth of uniform and clean two dimensional transition metal dichalcogenides. *Natl Sci. Rev.* **8**, nwa115 (2021).
53. Hoang, A. T. et al. Low-temperature growth of MoS<sub>2</sub> on polymer and thin glass substrates for flexible electronics. *Nat. Nanotechnol.* **18**, 1439–1447 (2023).
54. Mawlong, L. P. L. et al. Reduced defect density in MOCVD-grown MoS<sub>2</sub> by manipulating the precursor phase. *ACS Appl. Mater. Interfaces* **15**, 47359–47367 (2023).
55. Mak, K. F. et al. Tightly bound trions in monolayer MoS<sub>2</sub>. *Nat. Mater.* **12**, 207–211 (2013).
56. Liu, Y., Shen, T., Linghu, S., Zhu, R. & Gu, F. Electrostatic control of photoluminescence from A and B excitons in monolayer molybdenum disulfide. *Nanoscale Adv.* **4**, 2484–2493 (2022).
57. Ryu, G. H. et al. Effects of dry oxidation treatments on monolayer graphene. *2d Mater.* **4**, 024011 (2017).
58. Toh, C.-T. et al. Synthesis and properties of free-standing monolayer amorphous carbon. *Nature* **577**, 199–203 (2020).
59. Ma, Z. et al. Control of hexagonal boron nitride dielectric thickness by single layer etching. *J. Mater. Chem. C* **7**, 6273–6278 (2019).
60. Hong, S. et al. Ultralow-dielectric-constant amorphous boron nitride. *Nature* **582**, 511–514 (2020).
61. Zhang, B. Y. et al. Hexagonal metal oxide monolayers derived from the metal-gas interface. *Nat. Mater.* **20**, 1073–1078 (2021).



62. Chen, Q. et al. Lattice modulation strategies for 2D material assisted epitaxial growth. *Nano Converg.* **10**, 39 (2023).
63. Li, X. et al. Large-area synthesis of high-quality and uniform graphene films on copper foils. *Science* **324**, 1312–1314 (2009).
64. Kim, K. et al. Grain boundary mapping in polycrystalline graphene. *ACS Nano* **5**, 2142–2146 (2011).

### Acknowledgements

This study was supported by the Basic Science Research Program of the National Research Foundation of Korea (NRF-2021R1C1C2006785 and NRF-2022R1A2C4002559), Institute for Basic Science (IBS-R026-D1), and Yonsei University Research Fund (Post Doc. Researcher Supporting Program) of 2024 (project no.: 2024-12-0018).

### Author contributions

M.J. and M. Kim contributed equally to this work. K.K. conceived the project and provided guidance for the experiments and simulations. M.J., M. Kim, and K.K. wrote the manuscript with inputs from all authors. M.J. and M. Kim mainly conducted experiments, Monte Carlo simulations, and data analysis. S.L. assisted in conducting the simulations and sample characterizations. M. Kwon and H.K. conducted Raman and PL spectrum measurements. K.L., J.P., and Y.L. assisted in sample characterizations. A.T.H. and J.-H.A. synthesized and provided MOCVD MoS<sub>2</sub> samples.

### Competing interests

The authors declare no competing interests.

### Additional information

**Supplementary information** The online version contains

supplementary material available at <https://doi.org/10.1038/s41699-024-00473-w>.

**Correspondence** and requests for materials should be addressed to Kwanpyo Kim.

**Reprints and permissions information** is available at <http://www.nature.com/reprints>

**Publisher's note** Springer Nature remains neutral with regard to jurisdictional claims in published maps and institutional affiliations.

**Open Access** This article is licensed under a Creative Commons Attribution 4.0 International License, which permits use, sharing, adaptation, distribution and reproduction in any medium or format, as long as you give appropriate credit to the original author(s) and the source, provide a link to the Creative Commons licence, and indicate if changes were made. The images or other third party material in this article are included in the article's Creative Commons licence, unless indicated otherwise in a credit line to the material. If material is not included in the article's Creative Commons licence and your intended use is not permitted by statutory regulation or exceeds the permitted use, you will need to obtain permission directly from the copyright holder. To view a copy of this licence, visit <http://creativecommons.org/licenses/by/4.0/>.

© The Author(s) 2024